# Risk assessment in different Judo techniques for children and adolescent athletes

*Original*
Risk assessment in different Judo techniques for children and adolescent athletes / Vacca, L., Rosso, V., Gastaldi, L.. - In: PROCEEDINGS OF THE INSTITUTION OF MECHANICAL ENGINEERS. PART H, JOURNAL OF ENGINEERING IN MEDICINE. - ISSN 0954-4119. - 234:7(2020), pp. 686-696. [10.1177/0954411920915589]

*Publisher:*
SAGE Publications Ltd

*Published*
DOI:10.1177/0954411920915589

# Design and Analysis of High-Speed Induction Machines for Submerged Cryogenic Pumps

Marco Biasion, *Student Member, IEEE*
*Politecnico di Torino*
*Dipartimento Energia*
Torino, Italy
marco.biasion@polito.it

Gianluca Carena
*Vanzetti Engineering S.p.A*
*Product Engineering Department*
Cavallerleone (CN), Italy
carena@vanzettiengineering.com

Silvio Vaschetto, *Senior Member, IEEE*
*Politecnico di Torino*
*Dipartimento Energia*
Torino, Italy
silvio.vaschetto@polito.it

Alberto Tenconi, *Senior Member, IEEE*
*Politecnico di Torino*
*Dipartimento Energia*
Torino, Italy
alberto.tenconi@polito

Andrea Cavagnino, *Fellow, IEEE*
*Politecnico di Torino*
*Dipartimento Energia*
Torino, Italy
andrea.cavagnino@polito.it

***Abstract*—This paper discusses the electromagnetic design and loss analysis of a 15 kW, 13500 rpm induction machine for a single-stage submerged cryogenic pump. The study starts from an existing machine driving a three-stage cryogenic pump, rated 7.5 kW at 7300 rpm. The new motor design is approached by increasing the rotating speed of the reference machine at fixed outer diameter, aiming at an optimum between efficiency and power factor. Experimental investigations are carried out on the reference machine to analyze its thermal behavior. The results allow to obtain initial values for the electrical loadability of cryogenic induction machines. The electromagnetic design of the high-speed motor is successfully carried out with the help of detailed numerical simulations, particularly devoted to a precise analysis of the losses active in the machine. Special care is given to the iron losses, estimated with two different approaches.**

***Keywords*—Induction machines, cryogenics, liquid nitrogen, cooling, thermal design, machine design, loss analysis, magnetic iron losses, Finite-Element Method (FEM).***

## I. INTRODUCTION

Submerged cryogenic pumps are the key components of every facility for cryogenic fluids such as liquefied natural gas (LNG), liquid hydrogen ($LH_2$) and liquid nitrogen ($LN_2$) to name some. The electrical machine driving the pump operates submersed in the cryogenic environment, which provides an efficient cooling and an effective lubrication for the rolling bearings. The actual operating temperature of the machine depends on the cryogenic fluid and varies between 20 K ($LH_2$) and ~110 K (LNG). The operation in $LN_2$ at ~77 K is common for research and testing purposes [1]–[3].

Electrical machines for cryogenic pumps are normally manufactured using conventional materials such as copper or aluminum conductors and silicon-iron alloys. The electrical resistivity of conductors decreases significantly at cryogenic temperature, usually following a nonlinear behavior [4]. The magnetization properties of silicon-iron alloys may vary, depending on the operating temperature [5], while the power losses generally increase due to enhanced eddy current related loss phenomena [5], [6]. The insulating materials operate in a relatively safe environment, without experiencing partial discharge, corona, thermal aging and oxidation. However, a proper chemical composition must be adopted to ensure their performance and durability [7].

The simplified structure of a submerged cryogenic pump assembly is sketched in Fig. 1. All its internal parts are wetted by the cryogenic fluid, whose flow is divided into two paths: the pump and motor flow. The former is the actual pumped fluid flow, while the latter is responsible for the cooling of the motor and the lubrication of the bearings. The motor operates in an open cooling configuration, with a continuous exchange of the cryogenic fluid with the cryostat, or tank environment, through the housing (E1, E2) as well as the bearings (B1, B2). The outer surface of the motor is normally subjected to natural convection, and the fluid composition inside the machine may be a complicated mix of liquid and gas.

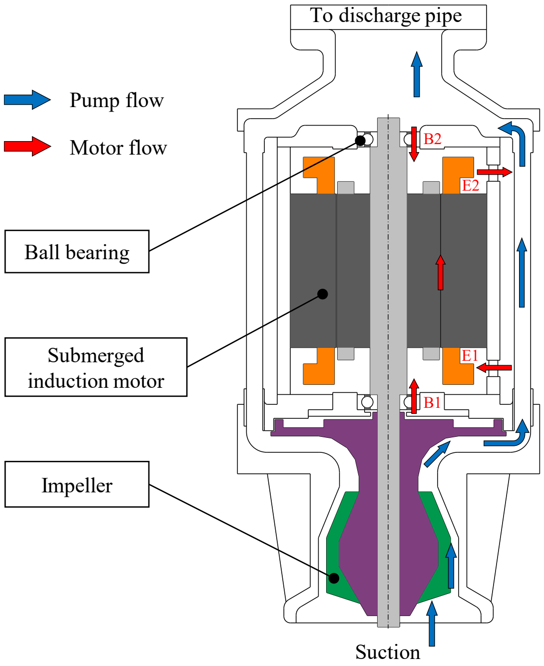

Fig. 1. Simplified structure of a single-stage submerged cryogenic pump. The motor flow serves as cooling flow in the motor and bearing lubrication.

Research efforts on the design and analysis of electrical machines for submerged cryogenic pumps have focused on cryogenic induction (IM) and permanent magnet (PM) motors of various types [8]–[12]. IMs were successfully employed in the early 1960s in missile propellant apparatuses operating with $LH_2$ [8]. Nowadays, they represent a consolidated solution for LNG submerged pump systems [2].

Cryogenic IMs, specifically for LNG facilities, have been employed in two- and four-pole configurations, operating at rotational speeds in the range ~3000 – 7000 rpm. The pump drive is normally operated under inverter supply with scalar control and limited or absent flux-weakening requirements.

Despite their popularity, a few design guidelines for cryogenic IMs have been presented to date in the literature, especially regarding their electrical loadability and thermal management. In addition, high-speed cryogenic IMs may become popular in those applications in which the reduction in volume and weight of the pump assembly is of paramount importance. Examples may be found in emerging applications in the aerospace industry, that are gaining more and more interest [3]. In this regard, since the milestone study published in [8], even fewer research efforts have been expended within the research community.

The present paper deals with the electromagnetic design and detailed loss analysis of a 15 kW, 13500 rpm cryogenic IM. The machine is intended for a submerged cryogenic pump with a single stage, that must be developed starting from an existing three-stage pump. The electrical machine driving the existing pump, rated 7.5 kW at 7300 rpm, is taken as reference for the study. The new machine is developed by increasing the rotational speed of the reference motor at fixed outer diameter. The evaporation of the liquid due to the motor losses must be minimized; hence, the design should target at limiting the temperature raise of the different parts of the motor. The goal is therefore to design a high-speed machine maximizing efficiency and power factor. All the studies presented in this research refer to a machine operating with $LN_2$. In the first part of the paper, two separate experimental investigations are carried out on the reference machine to analyze its thermal behavior and operating limits. The study aims at defining preliminary design guidelines in terms of admissible electrical loadability of cryogenic IMs. The second part of the work discusses the electromagnetic design of the high-speed motor, which is performed with analytical equations and considering tailored material stress indexes. Numerical simulations are devoted to a precise analysis of the losses active in the machine, giving special attention to the iron losses that are estimated with an advanced engineering approach.

## II. PRELIMINARY TESTS ON THE REFERENCE MACHINE

The design process of electrical machines is a demanding task and includes electromagnetic, thermal and mechanical constraints. During the electromagnetic design, the material stress indexes (airgap flux density, slot current density and linear current density) must be chosen depending on the adopted cooling strategy and accepted temperature rise in various machine parts. Thermal analyses constitute a valid approach to initiate studies on the operating limits of cryogenic machines, that undoubtedly operate in a quite particular environment.

### A. *Full load and overload test*

The reference machine was operated during the first test campaign at full load and overload under inverter supply. Fig. 2a depicts the test rig used for the experiments in $LN_2$. Fig. 2b details the motor flow and indicates the position of the PT100 cryogenic sensors used to record the temperature of the stator winding. The machine was designed to operate at rated load with an RMS stator current density $J_S = 7$ A/mm$^2$. Several test runs were performed at different load and speed values, operating the motor at $6 < J_S < 12$ A/mm$^2$.

The results showed that the sensors detected a negligible variation with respect to the inlet temperature (point E1 in Fig. 2b), that was stable at ~100 K. These findings must be critically interpreted. In case the sensors were not carefully placed in the slots, chances are that they detected the temperature of the cryogenic fluid instead of the winding temperature. It must be pointed out that the temperature at which the motor operated was higher than 77 K, since the pressure in the cryostat was higher than the ambient one.

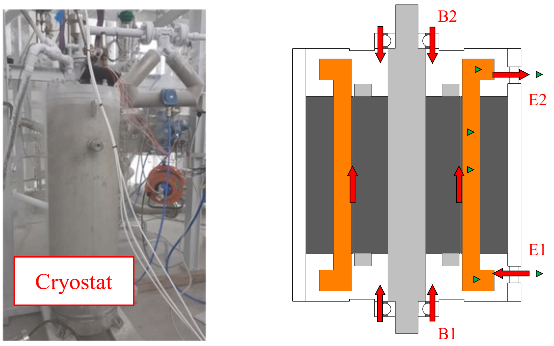

(a) (b)

Fig. 2. Experimental tests performed on the reference machine. (a) The test rig with the cryostat containing the pump submerged in $LN_2$; (b) sketch of the submerged machine detailing the flow path of $LN_2$ (motor flow). Pictured with green markers are the PT100 temperature sensors.

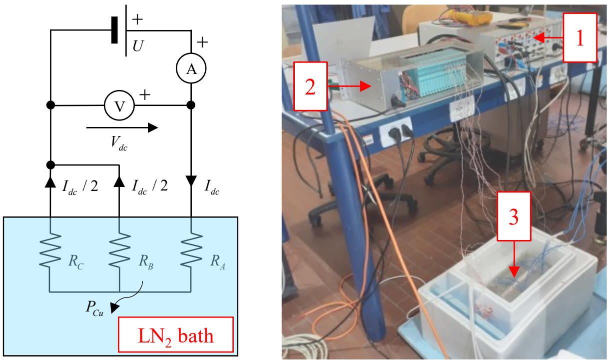

(a) (b)

Fig. 3. The average winding temperature test performed on the stator of the reference machine. (a) The electrical scheme; (b) the experimental setup. Detailed are the electrical connections (1), the data acquisition system for the PT100 sensors (2) and the stator immersed in $LN_2$ at 77 K (3).

### B. *Average winding temperature test*

The second test campaign aimed at verifying the readings of the temperature sensors, given their uncertain placement. The electrical scheme as well as the experimental setup used for the tests are depicted in Fig. 3a and Fig. 3b, respectively. The stator of the reference machine was immersed in $LN_2$ at 77 K and the average winding resistance was measured at different values of the dc supply current. The stator winding was connected as shown in Fig. 3a due to an inaccessible star point. From the test results, it was possible to determine the average stator winding temperature and correlate it to the dissipated loss by Joule effect. This allowed to preliminarily estimate values for the electrical loadability of cryogenic IMs.

Table I summarizes the results of the dc test. The dc resistance $R_{ave}$ was determined online starting from the measured power $P_{Cu}$ and the supply current $I_{dc}$. From the measured dc resistance of the circuit, the average winding temperature was computed using (1).

$$R_{ave} = R_{ref} \cdot \left( \rho_{ave} / \rho_{ref} \right) \tag{1}$$

TABLE I. RESULTS OF THE DC TEST AT DIFFERENT SUPPLY CURRENTS: AVERAGE WINDING TEMPERATURE AND OVERTEMPERATURE

| $I_{dc}$ (A) | $P_{Cu}$ (W) | $R_{ave}$ (mΩ) | $\theta_{ave}$ (K) | Δθ (K) |
|---|---|---|---|---|
| 7 | 4.5 | 91 (ref) | 77 | - |
| 20 | 37 | 91.4 | ~77 | 0 |
| 30 | 83 | 92.5 | 77.5 | 0.5 |
| 40 | 152 | 94.6 | 78.2 | 1.2 |
| 50 | 247 | 98.9 | 79.5 | 2.5 |
| 70 | 574 | 124 | 87 | 10 |

$R_{ref}$ = 91 mΩ is the reference value for the dc resistance, measured at 77 K and $I_{dc}$ = 7 A, prior to perform any test. $\rho_{ave}$ is the copper resistivity in Ω·m at the average winding temperature and $\rho_{ref}$ is the copper resistivity at 77 K. The values for the copper resistivity $\rho_{Cu}$ at cryogenic temperature were taken from [4], and fitted in the range $70 < \theta < 350$ K using (2).

$$\rho_{Cu} = 6.86 \cdot 10^{-11} \cdot \theta - 3.32 \cdot 10^{-9} \tag{2}$$

The average winding temperature increase Δθ = 10 K corresponded to a dissipation that was roughly one order of magnitude above the stator Joule loss of the reference motor at rated conditions. Values for the supply current above 70 A eventually led to the failure of the insulation of the winding, probably because of remarkable local thermal stresses in the winding, due to significantly higher Δθ. Also in this test, the PT100 sensors detected the temperature of the $LN_2$ bath.

The electrical loadability *AJ* is defined by means of the thermal loading per unit surface $p_{Cu}$. It represents the ratio between the stator Joule loss in the active parts (excluding the end winding dissipation) and the airgap surface (3).

$$p_{Cu} = \frac{P_{JS,a}}{S_\delta} = \frac{P_{JS,a}}{\pi \cdot D_{is} \cdot l} = \rho_{Cu} \cdot A_S \cdot J_S \tag{3}$$

$P_{JS,a}$ is the Joule loss of the active parts of the stator winding, $S_\delta$ is the airgap surface, $D_{is}$ is the inner stator diameter, $l$ is the stack length, $A_S$ and $J_S$ are the linear current density and the slot current density of the stator, respectively.

The electrical loadability was determined for the case in which Δθ = 10 K, i.e., when the average winding temperature was 87 K. The obtained value was $A_S J_S = 3 \cdot 10^4$ A$^2$/cm/mm$^2$, which is about one order of magnitude above the higher bound suggested in [13] for conventional liquid-cooled IMs.

The result on the electrical loadability should be taken as an upper bound. In fact, various factors influenced the results obtained with the presented test setup:

- The absence of both the rotor and the end shields (enhanced heat extraction at the inner stator surface).
- The unbalanced operation of the stator winding (half the supply current flowed in two of the three phases).
- The impossibility to detect hotspots in the winding.

Additional tests with an improved setup are necessary to provide more detailed guidelines on the electrical loadability. However, the tests highlighted the difficulties in measuring the winding temperature in cryogenic machines, and the necessity to pay particular care to the installation of the sensors in the slots.

TABLE II. DESIGN SPECIFICATIONS OF THE HIGH-SPEED MACHINE

| Parameter | Value | Unit |
|---|---|---|
| Rated power | 15 | kW |
| Rated torque | 11 | Nm |
| Rated frequency | 225 | Hz |
| DC link voltage | 540 | V |
| Number of poles | 2 | - |
| Number of phases | 3 | - |
| Connection | Star | - |
| Stator \| rotor slots | 24 \| 28 | - |
| Outer diameter | 135 | mm |
| Stack length | 85 | mm |
| Airgap thickness | 0.4 | mm |
| **Cooling method** | Flooded with external and internal $LN_2$ flow | |
| **Supply** | Inverter-fed with scalar control | |
| **Operation** | Continuous | |

## III. DESIGN OF THE HIGH-SPEED MACHINE

The use of high-speed submerged cryogenic pumps has been studied in missile propellant apparatuses since the early 1960s [8]. In those applications, there was little concern about a low-loss machine design, since the cryogenic fluid had to be gasified prior to burning. However, this might not be the case for other applications. The electric motor driving a general-purpose cryogenic pump must be designed in such a way that the losses, and therefore their heat generation, is minimized.

### *A. Design specifications and guidelines*

The main design specifications of the high-speed machine are listed in Table II. The design was carried out with well-established design rules for inverter-fed IMs, and without using optimization techniques. Technical considerations about the layout of the pump, together with cost constraints, fixed the main geometrical parameters of the high-speed machine.

Compared to the reference motor, the high-speed machine features the following design aspects:

- Same number of poles, phases and DC link voltage.
- Same stator (inner, outer) and shaft diameters.
- Reduced stack length and increased airgap thickness.
- Unskewed rotor slots (with a different geometry).
- Different winding layout.
- Higher grade (lower loss) core material.

The geometry of the reference and high-speed machines are compared in Fig. 4. The use of commercially available laminations was imposed for the high-speed design.

The choice of the same number of poles was to minimize the supply frequency given the rated speed requirement of the motor. The constraint on the outer diameter of the stator was imposed to fit the motor in the existing pump frame with minimum adjustments. The inner stator and shaft diameters were kept the same to accommodate bearings of the same dimensions, given the very similar design torque.

The higher rotational speed of the motor under design causes an increase in the airgap friction losses. Such increase, after having chosen the rotor diameter and speed, is roughly proportional to the stack length. Thus, the latter was reduced, considering the mechanical constraints associated to the construction of the pump, from 100 mm (reference machine) to 85 mm.

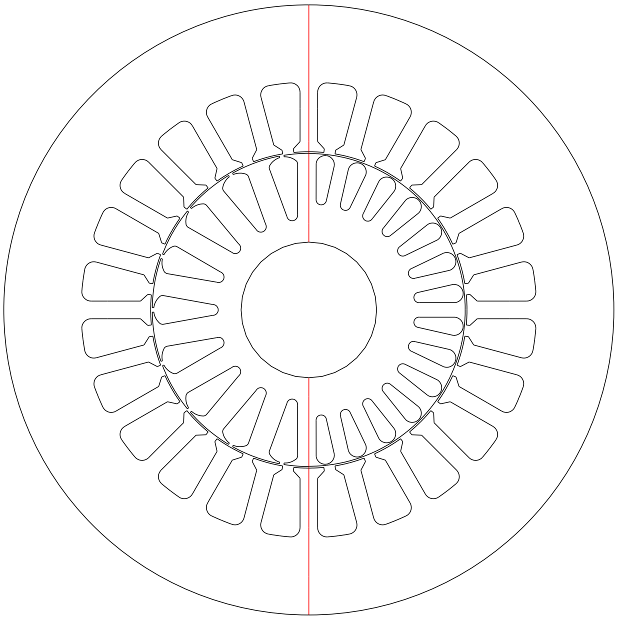

Fig. 4. The design of the high-speed cryogenic-cooled IM: comparison of the reference (left) and the proposed geometries (right).

A different slot geometry was selected for the design of the rotor laminations. Given the roughly doubled supply frequency, it was necessary to reduce the slot height to avoid a significant impact especially on the peak torque performance of the motor. Strictly speaking, there are usually quite limited requirements in terms of peak torque performance of IM for pump drives. However, it was decided to keep an ample margin with respect to the design torque. This in view of further developments of the motor performance, given the thermal and efficiency requirements as well as the actual application of the pump.

The number of rotor slots was chosen according to well-established rules for stator/rotor slot combinations without skewing (the reference machine was built with skewed rotor slots instead). Closed rotor slots may help to reduce the losses at the stator surface due to rotor slotting harmonics. However, the iron bridges tend to saturate easily at full load, and that benefit may be lost. The thickness of the airgap was therefore increased by 14% to partially counterbalance this effect. A slightly wider airgap generally provides a better damping effect to higher-order spatial and time harmonics, without significantly increasing the magnetizing current.

The stator of the reference motor was equipped with a full-pitch, single-layer distributed winding with two parallel paths. A similar arrangement, but in double-layer configuration and a with a short pitching of two slot pitches was selected for the high-speed design. This to reduce the impact of both the fifth and seventh spatial MMF harmonics.

The material grade chosen for the laminations was a low-loss M270-35A silicon-iron alloy. Its reduced lamination thickness would surely help to mitigate the enhanced eddy current related loss phenomena in soft ferromagnetic materials at cryogenic temperature [6]. For comparison, the iron core of the reference machine was manufactured with M530-50A silicon-iron alloys.

### *B. Assessment of different design alternatives*

After the selection of the lamination geometry, the design of the high-speed machine had to be completed by assigning proper stress indexes to the materials, i.e., the flux density in the iron parts and the current density in the stator and rotor conductors. The machine design should target at reaching the best possible efficiency; however, a good power factor should also be achieved to minimize the current rating of the power converter. The material stress indexes of the high-speed machine were therefore chosen aiming at the best trade-off design in terms of efficiency and power factor.

TABLE III. DESIGN ALTERNATIVES OF THE HIGH-SPEED MACHINE: STRESS INDEXES AND ELECTRICAL LOADABILITY (STATOR AND ROTOR)

| **Design** | **$B_\delta$ (T)** | **$J_S$ \| $J_R$ (A/mm$^2$)** | **$A_S$ \| $A_R$ (A/cm)** | **$A_S J_S$ \| $A_R J_R$ (A$^2$/cm/mm$^2$)** |
|---|---|---|---|---|
| D1 | 0.78 | 8.7 \| 7.7 | 385 \| 330 | 3359 \| 2537 |
| D2 | 0.72 | 8.8 \| 8.3 | 396 \| 358 | 3486 \| 2984 |
| D3 | 0.67 | 9.3 \| 9.0 | 419 \| 387 | 3881 \| 3482 |
| D4 | 0.62 | 9.9 \| 9.7 | 449 \| 416 | 4454 \| 4032 |
| D5 | 0.58 | 10.8 \| 10.4 | 483 \| 447 | 5193 \| 4646 |
| D6 | 0.55 | 11.8 \| 11.1 | 521 \| 478 | 6162 \| 5324 |
| D7 | 0.52 | 12.1 \| 11.9 | 564 \| 511 | 6817 \| 6073 |
| Comparison at defined torque (11 Nm) and machine geometry | | | | |

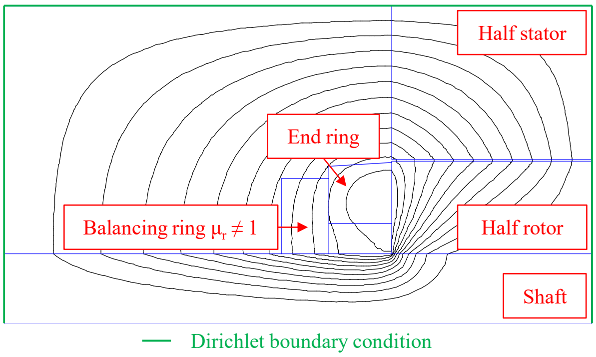

Fig. 5. Field plot obtained with the 2D nonlinear axisymmetric FEA model for to estimation of the end ring parameters.

Table III presents seven design alternatives evaluated analytically and obtained by various combinations of the stress indexes on the design plane, at fixed design torque and lamination geometry, see Fig. 4 (right). The alternatives were generated by changing the number of turns of the stator winding. It is noted that until design D5, the stress indexes, in particular the *AJ* product for the stator, are in line with those of conventional liquid-cooled IMs. This finding should not be misunderstood: the efficient and reliable design of cryogenic machines primarily aims at minimizing the heat generation, to prevent excessive evaporation of the cryogenic liquid, without necessarily maximizing the torque density.

The design alternatives were all verified through voltage-fed nonlinear 2D time-stepping finite element simulations (FEA). The finite-element domain was coupled to an external circuit to take the 3D end effects into account. The use of a 2D multi-slice FEA model was not necessary since the rotor is unskewed.

The 2D axisymmetric time-harmonic FEA model shown in Fig. 5 was employed to evaluate the parameters of the end ring of the rotor cage, particularly its self-inductance. Such approach has been recognized as more accurate with respect to analytical calculations [14]. In addition, this simulation allowed to take into consideration the influence on the end ring parameters of a mildly ferromagnetic balancing ring. The field problem was solved at the slip frequency, considering the nonlinear properties of the ferromagnetic materials (iron core and shaft) and zeroing their electrical conductivity.

The efficiency and the power factor of the different design alternatives were estimated numerically by FEA. The use of numerical simulations to determine the electromagnetic losses in the motor (stator Joule losses, rotor Joule losses, stator and rotor iron losses) allowed to account for the harmonic phenomena in the rotor cage and in the iron core as well as the additional losses due to the skin and proximity effect in the stator windings. The machine was simulated under sinusoidal voltage supply at 225 Hz, and each period was discretized in 512 time steps.

The losses as well as the machine performance were investigated considering preliminary values for the average conductor temperature. Considering the motor operating in a cryogenic environment at 100 K (as for the tests on the reference machine), the temperature of the stator winding and the rotor cage were set to 110 and 120 K, respectively. Difficulties were encountered in selecting proper material properties of aluminum. Thus, the data employed in [1] were chosen, due to the lack of information from experiments.

The Joule losses occurring in the FEA domain were evaluated at the post-processing stage with (4) and (5).

$$P_{JS,a} = R_{S,a} \cdot \sum_{m=1}^{3} I_{Sm}^2 \tag{4}$$

$$P_{JR} = \frac{1}{T} \int_T \left( \sum_{i=1}^{Q_R} \int_{V_b} \frac{\left|J_R\right|^2}{\sigma_b} dv \right) dt \tag{5}$$

$P_{JS,a}$ is the Joule loss of the active parts of the stator winding and $R_{S,a}$ is their resistance, $m$ is the number of phases, and $I_{Sm}$ is the RMS value of each phase current. $P_{JR}$ is the Joule loss of the rotor bars; $T$ is the time period, $Q_R$, $V_b$, $J_R$ and $\sigma_b$ are the number of bars, their cross-sectional area, current density and electrical conductivity, respectively. The losses occurring in the stator and rotor end regions were computed by the circuit coupled to the FEA domain.

Detailed FEA investigations evidenced a negligible influence of the skin and proximity effect on the stator winding losses. This was due to the adoption of thin wire strands during the definition of the winding specifications.

The estimation of the iron losses was carried out at the post-processing stage, based on a well-established two-term loss model segregating the total losses into the harmonic hysteresis (6) and dynamic contributions (7) [15].

$$P_{Fe,h} = k_h \cdot D \cdot \int_{V_C} \left[ \sum_{n}^{M} (nf) \cdot \left\{ B_{x,n}^2 + B_{y,n}^2 \right\} \right] dv \tag{6}$$

$$P_{Fe,d} = k_d \cdot D \cdot \int_{V_C} \left[ \sum_{n}^{M} (nf)^2 \cdot \left\{ B_{x,n}^2 + B_{y,n}^2 \right\} \right] dv \tag{7}$$

$P_{Fe,h}$, $P_{Fe,d}$ and $V_C$ are the total hysteresis loss, the total dynamic loss and the volume of the of the stator or rotor core. $n$ and $M$ denote the order and the number of the time harmonics of the flux density waveform, respectively. $B_{x,n}$ and $B_{y,n}$ are the amplitudes of the harmonic components of the flux density in the $x$ and $y$ direction. The constant loss coefficients $k_h$ and $k_d$ were obtained from characterizations on an M270-35A laminated core at cryogenic temperature, with the procedure presented in [6].

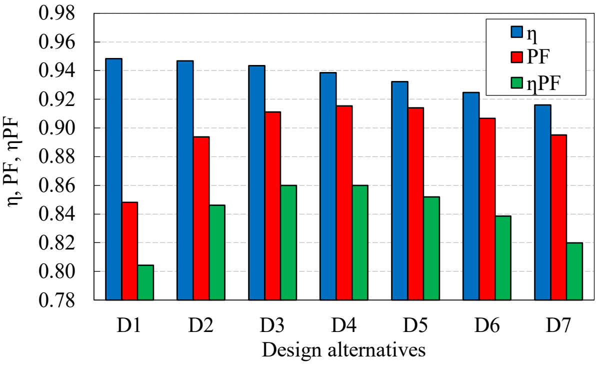

Fig. 6. The electromagnetic efficiency η, the power factor PF and their product ηPF. Computations based on time-stepping FEA.

The electromagnetic efficiency η and the power factor PF were evaluated with (8) and (9).

$$\eta = \frac{P_{out}}{P_{out} + P_{loss}} \tag{8}$$

$$\mathrm{PF} = P_{in} / S_{in} \tag{9}$$

$P_{out}$, $P_{in}$ and $S_{in}$ are the output and input active power, and the input apparent power, respectively. $P_{loss}$ represents the sum of all the electromagnetic losses.

Figure 6 summarizes the electromagnetic efficiency, the power factor and their product, estimated for all the design alternatives, see Table III. The best trade-off design is D4; its material stress indexes and electrical loadability are reported for convenience in the following.

- Airgap flux density $B_\delta = 0.62$ T.
- Stator slot current density $J_S = 9.9$ A/mm$^2$.
- Rotor bar current density $J_R = 9.7$ A/mm$^2$.
- Stator linear current density $A_S = 449$ A/cm.
- Rotor linear current density $A_R = 416$ A/cm.
- Electrical loadability (stator) $A_S J_S = 4454$ A$^2$/cm/mm$^2$.
- Electrical loadability (rotor) $A_R J_R = 4032$ A$^2$/cm/mm$^2$.

The validity of the chosen design D4 was confirmed by a comparative study. The reference and the proposed machine geometry (see Fig. 4) were compared in terms of their peak torque performance. Hence, the capability of the reference machine to operate at high speed was put under scrutiny. The comparison was carried out at the same design specifications, airgap flux density and stack dimensions, see Table II. The skewing of the rotor slots was considered for the reference machine.

Figure 7 details the comparison of the electromechanical characteristics obtained through analytical calculations. The peak torque performance of the design with the reference lamination geometry (RefGeo) is inferior to that of D4, because of their different rotor slot geometry. Additional analytical analyses also showed that the power factor was 5% lower for the RefGeo design.

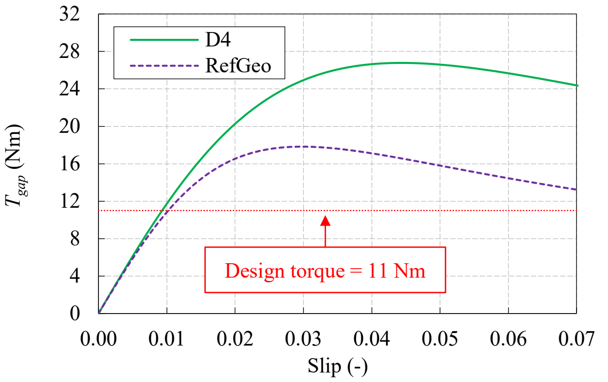

Fig. 7. Comparison of the electromechanical characteristics of the reference machine geometry (RefGeo) at high speed and the selected high-speed design (D4). Results obtained through analytical calculations.

### C. *Detailed loss analysis of design D4*

The preliminary estimation of the iron losses in the stator and rotor core of the high-speed machine relied on a model with constant loss coefficients. Such model was appropriate for the initial analyses carried out in section III.B, because of its fast and easy implementation. However, its accuracy may be limited in electrical machine applications [6], [16]. The model chosen for a detailed estimation of the iron losses was proposed in [16] and deeply analyzed in [6]. Here, the loss coefficients were variable with the frequency and flux density. The model was used for the computation of the stator iron losses, while the rotor iron losses were computed using a conventional approach with constant coefficients.

Figure 8 compares the results of the two loss models. The losses in all the considered stator iron parts are ~20% lower when computed using a variable coefficients approach, resulting in an overall 20% lower stator iron losses. The analysis of the results showed that the model with constant coefficients overestimated the dynamic loss component. The losses in the different parts of the stator are segregated into their hysteresis and dynamic components in Fig. 9. The dynamic losses largely prevailed, especially in the tooth-tips and teeth regions. This agrees with the physics of laminations excited with a relatively high fundamental frequency and subjected to several higher-order harmonics.

Figure 10 illustrates the segregation of the electromagnetic loss components active in the machine. The total Joule losses prevailed on the total iron losses, with a large share attributed to the rotor Joule losses. Also, a significant part of the total iron losses was concentrated in the rotor core.

The accurate estimation of the electromagnetic losses in cryogenic machines, particularly in high-speed cryogenic IMs, is a very demanding task and constitutes an open issue to the research community. The major difficulties are in estimating the temperature of the active parts in the actual operating conditions of the machine. Besides, the existing literature considerably lacks reliable and well documented results of experiments carried out on similar machines.

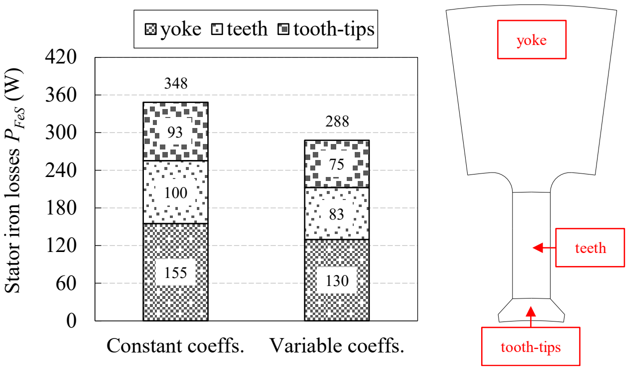

Fig. 8. High-speed design D4: iron losses at full load in different parts of the stator, determined by two different approaches. Detailed on the right, the computation domains represented in one slot pitch.

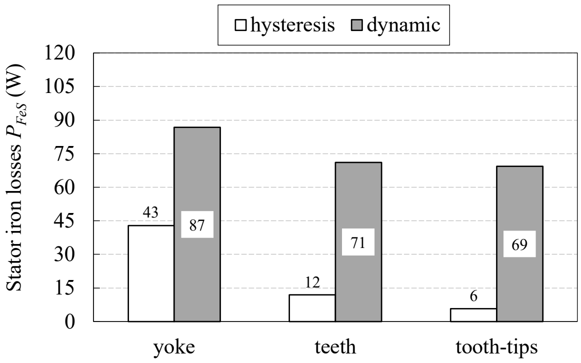

Fig. 9. High-speed design D4: separation of the iron losses into components in different parts of the stator core by the variable coefficients approach.

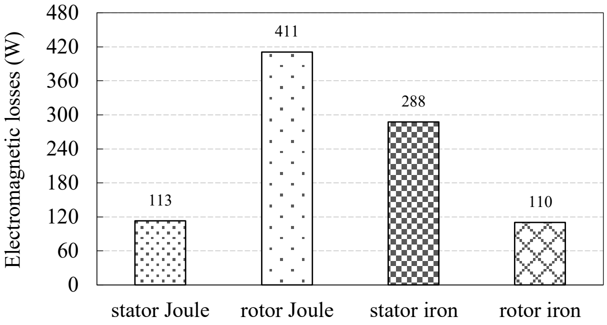

Fig. 10. High-speed design D4: segregation of the electromagnetic losses.

## IV. Conclusion

The present paper discussed the electromagnetic design and detailed loss analysis of a 15 kW, 13500 rpm IM for a single-stage submerged cryogenic pump, developed starting from a three-stage pump. The electrical machine driving the existing pump was taken as reference for the study. The new machine was developed by increasing the rotational speed of the reference motor at fixed outer diameter. The design targeted at limiting the temperature raise of the different parts of the machine to reduce the evaporation of the cryogenic liquid surrounding the device.

The first part of the work focused on two different experimental analyses devoted to the investigation of the thermal behavior of the reference machine. The results highlighted the difficulties in measuring the temperature of the winding in cryogenic machines. However, preliminary guidelines for the choice of the electrical loadability were provided in the study.

The second part of the work presented the details of the electromagnetic design of the high-speed machine. Suitable material stress indexes and a dedicated rotor geometry were proposed and investigated by assessing various design alternatives. The design featuring the best efficiency and power factor was selected. The simulation results showed that the proposed design was superior to the adaptation of the existing reference machine for a higher rotational speed. Detailed analyses of the electromagnetic loss phenomena of the designed machine particularly focused on the iron losses, that were estimated by an advanced approach.

The prototype of the high-speed machine based on the selected design is currently under construction and future research activities will focus on its experimental validation. Simplified thermal analyses and more detailed material characterizations are also under development. The ultimate aim of the ongoing study is to fill the gap existing in the literature about the strategies for the appropriate design, analysis and modeling of electrical machines for submerged cryogenic pump drives.

## REFERENCES

[1] L. F. D. Bucho, J. F. P. Fernandes, M. Biasion, S. Vaschetto, and A. Cavagnino, “Experimental Assessment of Cryogenic Cooling Impact on Induction Motors,” *IEEE Trans. Energy Convers.*, vol. 37, no. 4, pp. 2629–2636, Dec. 2022.

[2] M. Biasion, F. P. J. Fernandes, P. J. da Costa Branco, S. Vaschetto, A. Cavagnino, and A. Tenconi, “A Comparison of Cryogenic-Cooled and Superconducting Electrical Machines,” in 2021 IEEE Energy Conversion Congress and Exposition (ECCE), Oct 2021, pp. 4045–4052.

[3] F. Marignetti and G. Rubino, “Perspectives on Electric Machines with Cryogenic Cooling,” *Energies*, vol. 16, no. 7, p. 2994, 2023.

[4] H. J. Hucek, K. E. Wilkes, K. R. Hanby, and J. K. Thompson, *Handbook on materials for superconducting machinery*, Battelle Columbus Labs., OH. Metals and Ceramics Information Center, 1977.

[5] X. Pei, A. C. Smith, L. Vandenbossche, and J. Rens, “Magnetic Characterization of Soft Magnetic Cores at Cryogenic Temperatures,” *IEEE Trans. Appl. Supercond.*, vol. 29, no. 5, pp. 1–6, Aug. 2019.

[6] M. Biasion, I. S. P. Peixoto, J. F. P. Fernandes, S. Vaschetto, G. Bramerdorfer, and A. Cavagnino, “Iron Loss Characterization in Laminated Cores at Room and Liquid Nitrogen Temperature,” in 2022 IEEE Energy Conversion Congress and Exposition (ECCE), IEEE, Oct. 2022, pp. 1–8.

[7] R. Shively, “Submerged cryogenic motor materials development,” *IEEE Elect. Insul. Mag.*, vol. 19, no. 3, pp. 7–11, May/Jun. 2003.

[8] J. H. Redmond and F. W. Bott, “Development of cryogenic electric motors,” *SAE Trans.*, vol. 72, pp. 257–268, 1964.

[9] L. Dlugiewicz, J. Kolowrotkiewicz, W. Szelag, M. Baranski, and R. Neumann, “Electrical motor for liquid gas pump,” in International Symposium on Power Electronics, Electrical Drives, Automation and Motion, 2006, SPEEDAM, Taormina 2006.

[10] H. M. Kim, K. W. Lee, J. H. Park, and G. S. Park, “Design of cryogenic induction motor submerged in liquefied natural gas,” *IEEE Trans Magn.*, vol. 54, no. 3, pp. 1–4, March 2018.

[11] C. Guo, S. Huang, J. Wang, and Y. Feng, “Research of cryogenic permanent magnet synchronous motor for submerged liquefied natural gas pump,” *IEEE Trans. Energy Convers.*, vol. 33, no. 4, pp. 2030–2039, Dec. 2018.

[12] S. Liu, B. Ge, D. Tao, Y. Wang, P. Hou, and Y. Wang, “Research on the Influence of Power-Supply Mode and Copper-Shielding Layer on the Loss of Cryogenic Permanent Magnet Motor for LNG Pump,” *Energies*, vol. 15, no. 13, p. 4822, 2022.

[13] T. Jokinen, V. Hrabovcova, and J. Pyrhonen, *Design of rotating electrical machines*. John Wiley & Sons, 2013.

[14] K. Hameyer and R. Belmans, *Numerical modelling and design of electrical machines and devices*, vol. 1. WIT press, 1999.

[15] H. Domeki *et al.*, “Investigation of benchmark model for estimating iron loss in rotating machine,” *IEEE Trans Magn.*, vol. 40, no. 2, pp. 794–797, March 2004.

[16] E. Dlala, M. Solveson, S. Stanton, and A. Arkkio, “Improved model for the prediction of core loss in finite element analysis of electric machines,” in 2015 IEEE International Electric Machines & Drives Conference (IEMDC), May 2015, pp. 340–344.